Nanoscale

PAPER

View Article Online
View Journal | View Issue

Cite this: *Nanoscale*, 2022, **14**, 1807

Selective sequential infiltration synthesis of ZnO in the liquid crystalline phase of silicon-containing rod-coil block copolymers†

Ling-Ying Shi, *[a,b] Ashwanth Subramanian, [c] Lin Weng,[a] Sangho Lee, [b] Kim Kisslinger,[d] Chang-Yong Nam *[c,d] and Caroline A. Ross *[b]

Received 15th September 2021,
Accepted 12th November 2021

DOI: 10.1039/d1nr06065a

rsc.li/nanoscale

The combination of block copolymer (BCP) thin film self-assembly and selective infiltration synthesis of inorganic materials into one BCP block provides access to various organic–inorganic hybrids. Here, we apply sequential infiltration synthesis, a vapor-phase hybridization technique, to selectively introduce ZnO into the organic microdomains of silicon-containing rod-coil diblock copolymers and a triblock terpolymer, polydimethylsiloxane (PDMS)-*b*-poly{2,5-bis[(4-methoxyphenyl)-oxycarbonyl]styrene} (PDMS-*b*-PMPCS) and PDMS-*b*-polystyrene-*b*-PMPCS (PDMS-*b*-PS-*b*-PMPCS), in which the PMPCS rod block is a liquid crystalline polymer. The in-plane cylindrical PDMS-*b*-PMPCS and core–shell cylindrical and hexagonally perforated lamellar PDMS-*b*-PS-*b*-PMPCS films were infiltrated with ZnO with high selectivity to the PMPCS. The etching contrast between PDMS, PS and the ZnO-infused PMPCS enables the fabrication of ZnO/SiO_x binary composites by plasma etching and reveals the core–shell morphology of the triblock terpolymer.

Introduction

Films with chemically and geometrically ordered three-dimensional nanostructures are important in electronics, chemical separations, and energy conversion and storage.[1,2] Self-assembly of block copolymers (BCPs) is capable of producing ordered patterns with diverse geometries at length scales of ~5 nm and above, making them useful for such applications.[3–7] To broaden the scope of their functionality, BCP microdomains have been widely used as scaffolds for the growth of other materials through various liquid- and gas-phase processes. Examples include the use of hydrogen bonding or electrostatic interaction of species in a liquid-phase precursor solution to deposit metals selectively within microdomains[8–10] and sequential infiltration synthesis (SIS), a block-selective vapor-phase infiltration (VPI) technique based on atomic layer deposition (ALD).[11–14]

VPI can insert inorganic components into polymer films to form nanocomposites, and it has been utilized to improve etch resistance for nanofabrication, to enhance electron-density contrast for structural characterization, to improve optical, electrical and mechanical properties, and to modify the surface energy.[11,15] In particular, SIS infiltrates inorganic materials selectively into specific microdomains of self-assembled BCP films.[14,16–18] SIS has been used to enhance the etch contrast between blocks enabling two-dimensional and three dimensional nanofabrication where the BCP template is used as a sacrificial scaffold,[19–21] and to generate ordered functional inorganic–organic nanocomposites such as hybrid photovoltaics.[22]

In SIS, the selective growth of inorganic species occurs within polar blocks such as poly(methyl methacrylate) (PMMA) or poly(vinylpyrrolidone).[13,23,24] Blocks which contain carbonyl groups can be selectively infiltrated with metal oxides due to the interaction between the electrophilic metal atom in the precursor and the nucleophilic oxygen atom of the carbonyl group during sequential exposure to vapor-phase organometallic precursors such as trimethylaluminum (TMA) and water. Other carbonyl-containing polymers include polylactide (PLA), polyamide-6, poly(acrylic acid), and poly(ethylene terephthalate).[23] Most SIS studies involve PMMA-containing BCPs, but many functional liquid crystalline polymers also contain abundant carbonyl groups in their repeat units, making them potential candidates for SIS.

[a]*College of Polymer Science and Engineering, Sichuan University, Chengdu 610065, China. E-mail: shilingying@scu.edu.cn*
[b]*Department of Materials Science and Engineering, Massachusetts Institute of Technology, 77 Massachusetts Avenue, Cambridge, Massachusetts 02139, USA. E-mail: caross@mit.edu*
[c]*Department of Materials Science and Chemical Engineering, Stony Brook University, New York 11794, USA*
[d]*Center for Functional Nanomaterials, Brookhaven National Laboratory, New York 11973, USA. E-mail: cynam@bnl.gov*

†Electronic supplementary information (ESI) available: Additional cross-sectional SEM and TEM images of DM and DSM thin films before ZnO infiltration and TEM imaging and EDS mapping of films after ZnO infiltration. See DOI: 10.1039/d1nr06065a

Silicon-containing BCPs consist of an organic block combined with a silicon-containing block such as PDMS (polydimethylsiloxane), PFS (polyferrocenylsilane), POSS (polyoctahedral silsesquioxanes) or PDMSB (polydimethylsilacyclobutane), and possess an inherent etch contrast and high interaction parameter (χ) making them attractive for nanofabrication of structures with period below ~20 nm.[5,25–29] Guiding the self-assembly can yield ordered, non-bulk morphologies.[5] We previously used SIS to selectively deposit ZnO into one organic microdomain (PLA) of a silicon-containing triblock terpolymer, PDMSB-*b*-PS-*b*-PLA where PS represents polystyrene, producing three-dimensional (3D) organic/metal oxide/SiO_x composites after etching, and helping to resolve the 3D morphology of lamellar and perforated lamellar morphologies.[30] However, the ZnO formed nanoparticles within the PLA rather than a uniform distribution and ZnO was also present in the PDMSB, attributed to prior atmospheric oxidation of the Si in that block. There have not been other investigations combining SIS with a Si-containing BCP.

In this work, we demonstrate the SIS of ZnO into the organic liquid crystalline block of silicon-containing liquid crystalline diblock copolymers and a triblock terpolymer: polydimethylsiloxane (PDMS)-*b*-poly{2,5-bis[(4-methoxyphenyl)-oxycarbonyl]styrene} (PDMS-*b*-PMPCS, or DM) and PDMS-*b*-PS-*b*-PMPCS (DSM).[31–33] The PMPCS, a mesogen-jacketed liquid crystalline polymer,[34,35] displays an extended-chain conformation and forms a columnar nematic liquid crystalline phase. It contains two carbonyl groups in each side group of the repeat units, facilitating SIS. The high χ parameter and the liquid crystalline behavior of the DM and DSM promote the formation of various ordered nanostructures, and the nanostructures can be regulated by changing the composition of copolymers, varying the annealing temperature as well as changing the solvent composition for solvent vapor annealing.[31–33,36,37] The coil–coil–long-rod shape DSM triblock terpolymer with the interaction strength sequence, $\chi_{DM} > \chi_{DS} > \chi_{SM}$ ensures the formation of core–shell phase-separated nanostructures.[33,37] DM and DSM provide abundant well-ordered nanostructures with small feature sizes and specific morphologies such as zig-zag cylinders.[31–33,36] We carried out the ZnO SIS within both cylindrical-morphology DM and cylindrical and perforated lamellar DSM BCPs. The morphologies of the infiltrated composites were characterized by cross-sectional transmission electron microscopy (TEM) and elemental mapping using energy-dispersive spectroscopy (EDS). ZnO selectively infiltrates the PMPCS microdomains with high fidelity, which enhances the contrast between the PS and PMPCS and reveals the core–shell nanostructures of the DSM terpolymer. Compared with ZnO infiltration into the crystalline PLA microdomains of PDMSB-*b*-PS-*b*-PLA in our previous work,[30] the ZnO infiltration in this work demonstrated much improved uniformity and selectivity within the liquid crystalline PMPCS microdomains, and cylindrical as well as core–shell cylindrical and perforated lamellar ZnO/BCP composites were produced.

Experimental methods

BCP thin film deposition and solvent vapor annealing

The PDMS-*b*-PMPCS (DM) diblock copolymer and PDMS-*b*-PS-*b*-PMPCS (DSM) triblock terpolymer were synthesized by atom transfer radical polymerization.[31,33] Solutions of $D_{4K}M_{8K}$, $D_{4K}M_{12K}$ and $D_{4K}S_{7K}M_{40K}$ BCPs were made in toluene with concentration 3.0–4.0 wt%, where the subscripts represent the block molecular weight. $D_{4K}M_{8K}$, $D_{4K}M_{12K}$, and $D_{4K}S_{7K}M_{40K}$ films with thickness 40–80 nm were fabricated by spin-coating of the BCP solutions on PS brush-functionalized silicon substrates. The film thickness was measured by reflectometry (FilMetrics F20-UV, wavelength range of 300–1000 nm). The films were annealed to form ordered nanostructures by solvent vapor annealing with an acetone/heptane mixture as reported in previous work.[32,33] Based on the solubility parameters of the PDMS (δ_{PDMS} = 15.1 $MPa^{1/2}$) and PMPCS (δ_{PMPCS} = 20.8 $MPa^{1/2}$), acetone (δ_{ace} = 19.8 $MPa^{1/2}$) and heptane (δ_{hep} = 15.2 $MPa^{1/2}$) are selective for PMPCS block and PDMS block respectively, therefore the resulting BCP morphology depends on the solvent vapor composition.[32,33] Solvent vapor annealing was carried out by supporting the samples on a stage within a closed chamber of volume 80 cm^3 containing 6 mL of liquid acetone or acetone/heptane mixture for more than 3 h. The chamber had a loosely fitted lid that allowed the vapor to leak out slowly at room temperature, 23 ± 2 °C, with humidity 76%. In-plane cylindrical morphologies of the $D_{4K}M_{8K}$ and $D_{4K}M_{12K}$ were induced by solvent vapor annealing (SVA) using the vapors from an acetone/heptane volumetric ratio ~9 : 1 and 8 : 1 whereas in-plane cylindrical and perforated lamellar structures of the $D_{4K}S_{7K}M_{40K}$ triblock terpolymer were induced using the vapors from an acetone/heptane volumetric ratio 5 : 1 and 3.5 : 1, respectively. The swelling ratio of the films during SVA was 1.9–2.0, and the films were slowly dried at the end of the SVA by removing from the chamber.

Morphology characterization of BCP films

A two-step reactive ion etch (RIE, Plasma-Therm 790) was used to convert the BCP patterns to oxidized PDMS patterns. The etch process consisted of a 50 W CF_4 plasma at 15 mTorr for 5 s to remove the PDMS wetting layer on the surface and a 90 W O_2 plasma at 6 mTorr for 8–10 s to selectively etch the PMPCS and PS matrix. Imaging of the etched films was performed on a Zeiss Merlin scanning electron microscope (SEM), with 2–5 keV accelerating voltage, ~4 mm working distance and 100–150 pA beam current. For cross-sectional imaging, microscopy was performed on the Zeiss Merlin similarly to above with the sample held at an angle of 80°.

ZnO SIS and structural characterization of ZnO infiltrated BCP films

The SIS used metal precursors diethylzinc (DEZ) and trimethylaluminum (TMA) in a Cambridge Nanotech Savannah S100 ALD system at 85 °C. A single AlO_x priming cycle was performed (TMA exposure at ~12 Torr for 100 s, nitrogen purging at 100 sccm for 100 s, oxidation using water vapor at ~10 Torr

for 100 s, then a second nitrogen purge) then six ZnO infiltration cycles (DEZ exposure at ~1.7 Torr for 360 s, nitrogen purging at 100 sccm for 120 s, oxidation using water vapor at ~10 Torr for 360 s, then a second nitrogen purge). TEM characterization was carried out in a JEOL 2100, 200 kV; and scanning TEM (STEM) in an FEI Talos F200X at 200 kV with EDS elemental mapping. Cross-sectional TEM samples were prepared by Ga ion milling in a FEI Helios 600 Nanolab focused ion beam system.

Results and discussion

The three block copolymers $D_{4K}M_{8K}$, $D_{4K}M_{12K}$ and $D_{4K}S_{7K}M_{40K}$ used in this study are described in Table 1. The side group in each repeat unit (Fig. 1a) contains two carbonyl groups, and the bulky side groups closely linked to the backbone enforce the rigidity of the PMPCS chain and its liquid crystalline behavior.[34] In-plane cylindrical (IP-C) $D_{4K}M_{8K}$ and $D_{4K}M_{12K}$ and core–shell cylindrical and hexagonally perforated (HPL) $D_{4K}S_{7K}M_{40K}$ morphologies were selected for the SIS process.[31] Fig. 1b–e shows top-view SEM images of the films after oxygen plasma etching, in which the organic blocks are removed and the oxidized PDMS patterns show as bright contrast. The top-view image of $D_{4K}M_{12K}$ shows a partially gyroid-like domain morphology, but the cross-section image (inset) confirms the IP-C morphology throughout the majority of the film. The SEM images in Fig. 1b–e (inset) show the cross-sectional morphology of the IP-C perpendicular to the cylinders, and cross-sections parallel to the cylinders present line patterns, Fig. S1.† The film thicknesses are labeled in the insets of Fig. 1b–e.

We use SIS to place ZnO selectively within the PMPCS microdomains in order to enhance the etch resistance of the PMPCS domains for producing binary nanocomposites, and to visualize the core–shell morphology of the DSM triblock terpolymer. The infiltration consisted of an initial single AlO_x cycle using TMA and water (*i.e.*, AlO_x priming to improve the ZnO SIS fidelity) and six cycles of ZnO infiltration using DEZ and water. The gaseous reactants, TMA or DEZ and water, diffuse through the BCP film and react with active sites within the materials.[13] Because the weak Lewis-acidic DEZ cannot easily

Table 1 Molecular characteristics of the DM and DSM block copolymers used in this work

Sample	$M_{n(PDMS)}$ [a] (g mol^{-1})	$M_{n(PMPCS)}$ [a] (g mol^{-1})	PDI[b]	f_D [a] (%)	f_M [a] (%)	Morphologies selected for ALD	Period[c] (nm)
$D_{4K}M_{8K}$	4300	8100	1.05	43	57	IP-C	16.8
$D_{4K}M_{12K}$	4300	11 700	1.07	33	67	IP-C	14.7
$D_{4K}S_{7K}M_{40K}$	4300	40 500	1.07	11	73	IP-C	31.0
$D_{4K}S_{7K}M_{40K}$	4300	40 500	1.07	11	73	HPL (LAM$\parallel$, HEX$_\perp$)	16, 37

[a] Determined from ^{1}H NMR results of the macroinitiator and the block copolymers. [b] Determined from GPC using linear polystyrene standards. [c] Determined from SEM of etched films. PDI is the polydispersity and f_M is the volume fraction of PMPCS.

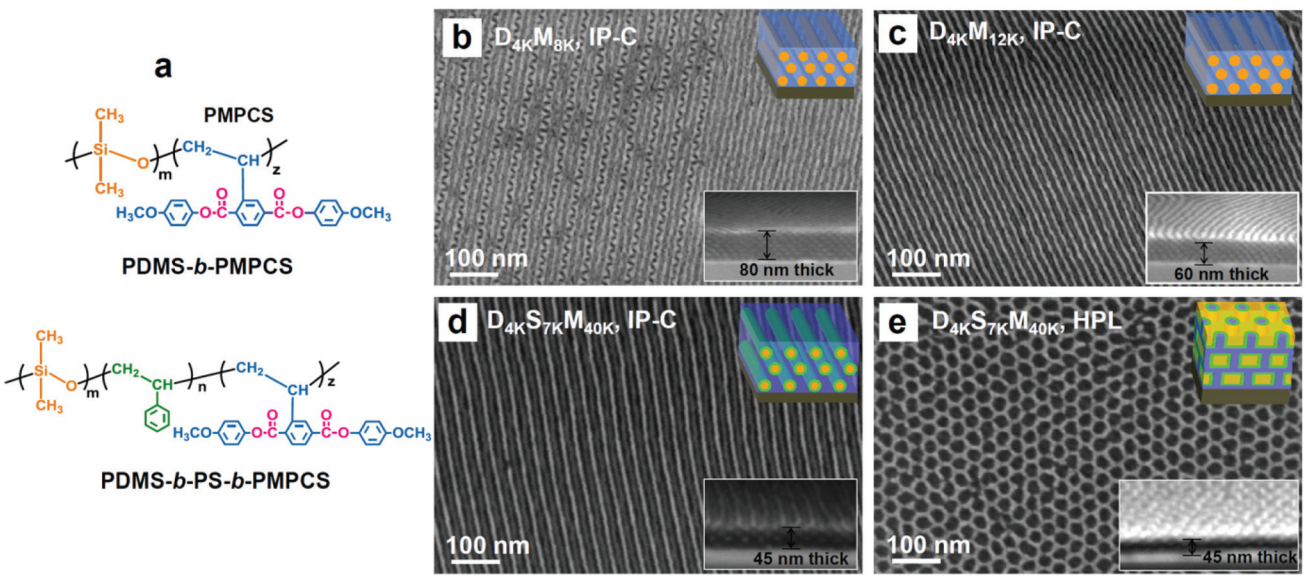

Fig. 1 (a) Chemical structures of the DM and DSM BCPs, and (b–e) top-view SEM images of oxidized PDMS patterns from thin films of in-plane cylindrical (b) $D_{4K}M_{8K}$ and (c) $D_{4K}M_{12K}$, and (e) in-plane cylindrical and (f) perforated lamellar $D_{4K}S_{7K}M_{40K}$. The insets show cross-sectional SEM images and structural illustrations (orange: PDMS, green: PS, blue: PMPCS).

react with the carbonyl groups, the AlO_x priming is necessary to generate –Al–OH species in the PMPCS microdomain through reaction of the more Lewis-acidic TMA with the Lewis-basic carbonyl group.[14,30,38] The –Al–OH species react with DEZ during the following infiltration cycles. The film is then exposed to an oxidizing agent, and the organometallic precursor is transformed into ZnO. The process was carried out at 85 °C, which is lower than the glass transition temperature of PMPCS (110–115 °C), hence the infiltration is not expected to influence the SVA-induced morphology of the thin film.

Fig. 2a and b illustrates the in-plane hexagonally packed cylinders (HEX) of DM thin films before and after infiltration synthesis. Before ZnO infiltration, the top-view SEM images of the $D_{4K}M_{8K}$ (f_{PDMS} 43%) and $D_{4K}M_{12K}$ (f_{PMPCS} 33%) thin films present an IP-C morphology with a cylinder–cylinder distance (L_0) of 14.7 nm and 16.8 nm, respectively (Fig. 2, top row). The cross-sectional SEM images display 9 layers of cylinders in the 80 nm thick $D_{4K}M_{8K}$ film and 6 layers of cylinders in the 60 nm $D_{4K}M_{12K}$ film. After ZnO-infiltration, the cross-sectional bright-field TEM images of $D_{4K}M_{8K}$ and $D_{4K}M_{12K}$ films also present grating patterns, Fig. 2b. The bright lines are the microdomains of the PDMS block, and the darker domains are ZnO-infiltrated PMPCS. The TEM grating patterns show a higher frequency compared to the SEM images with spacings (L') of 8.2 nm and 9.6 nm for the $D_{4K}M_{8K}$ and $D_{4K}M_{12K}$, respectively. The TEM sample is cut parallel to the cylinders along plane A of Fig. 2b, and the projection of cylinders is illustrated by the red and grey lines which represent the cylinders in different layers. According to the geometry of a HEX structure, L' should be $\sqrt{3}L_0/2$. However, L' is less than the corresponding $\sqrt{3}L_0/2$ value (12.7 nm for $D_{4K}M_{8K}$ and 14.5 nm for $D_{4K}M_{12K}$), which is consistent with the distortion of the HEX structure due to the reduction of the film thickness during the deswelling.[36,39] The distortion parameters ($L'/(\sqrt{3}L_0/2)$) are 0.65 and 0.66 for $D_{4K}M_{8K}$ and $D_{4K}M_{12K}$, respectively. This can be compared with a distortion factor of 0.62 for the in-plane HEX structure of a PS-*b*-PDMS thin film annealed in toluene/heptane vapor and slowly dried.[40] The large distortion occurs because the chain mobility is insufficient during the drying to allow the microdomains to reorganize as the film volume decreases, so the structure shrinks along the out-of-plane direction while maintaining its in-plane spacing.

The cross-sectional image of ZnO-infiltrated $D_{4K}M_{8K}$ shows better contrast than that of the $D_{4K}M_{12K}$, which is attributed to the higher volume fraction of the PDMS block in $D_{4K}M_{8K}$. Due to the overlap of the PMPCS/ZnO matrix and PDMS cylinders, EDS composition mapping along the cross-section presents insufficient resolution to resolve the morphology (Fig. S2 and 3†), but overall ZnO infiltration is confirmed. From the TEM image and EDS mapping, the ZnO infiltration in the PMPCS is quite uniform without the larger crystals seen in the PLA block of ref. 25. The number of layers of cylinders in the cross-sectional TEM image is consistent with that observed in the cross-sectional SEM images.

We now describe ZnO infiltration in the DSM triblock terpolymer films. The DSM exhibits Flory–Huggins parameters in the order $\chi_{DM} > \chi_{DS} > \chi_{SM}$,[33] which promotes core–shell structures to minimize contact between the PDMS and PMPCS. However, both PS and PMPCS are removed by plasma etching and the film only presents oxidized PDMS patterns. The selective deposition of ZnO in the PMPCS domain provides an opportunity to resolve the morphologies of the PMPCS and PS microdomains.

Fig. 3a schematically depicts ZnO infiltration in the proposed DSM core–shell cylindrical structure. The morphology of the film was characterized by bright-field TEM imaging, high-angle annular dark-field (HAADF) STEM imaging and EDS elemental mapping. Fig. 3b displays the morphology of the cross-sections perpendicular to the cylinders along plane B, and the bright-field TEM image of the cross-sections. The dark

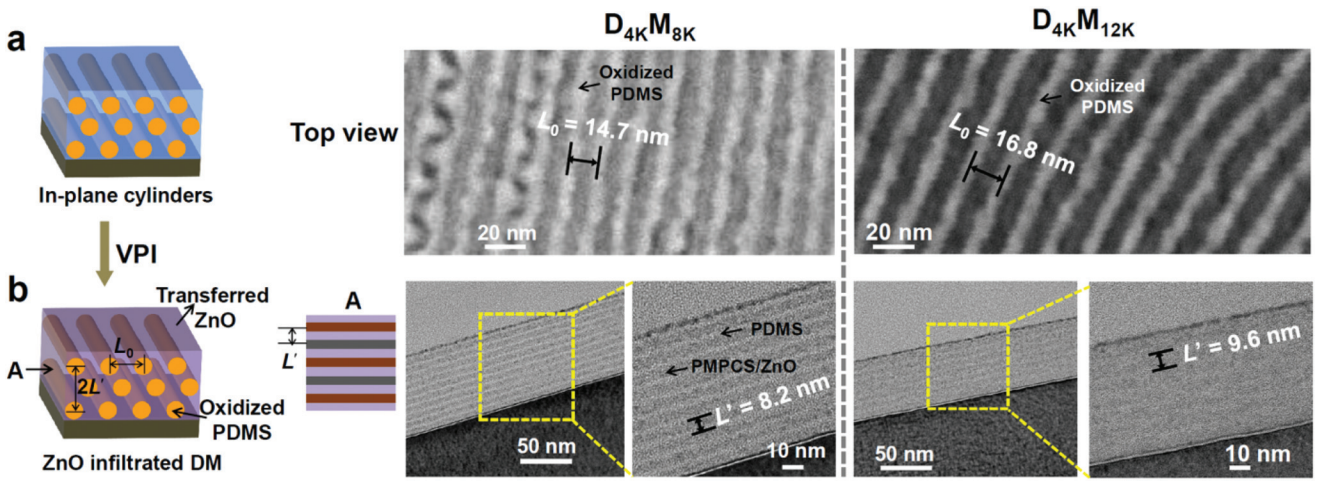

Fig. 2 ZnO infiltration in in-plane cylindrical DM films: (a) the structure and top-view SEM images of oxidized PDMS patterns of $D_{4K}M_{8K}$ and $D_{4K}M_{12K}$ thin films before ZnO infiltration with an indication of the cylinder-to-cylinder distance; (b) structural illustration and cross-sectional bright-field TEM images of corresponding films after ZnO infiltration.

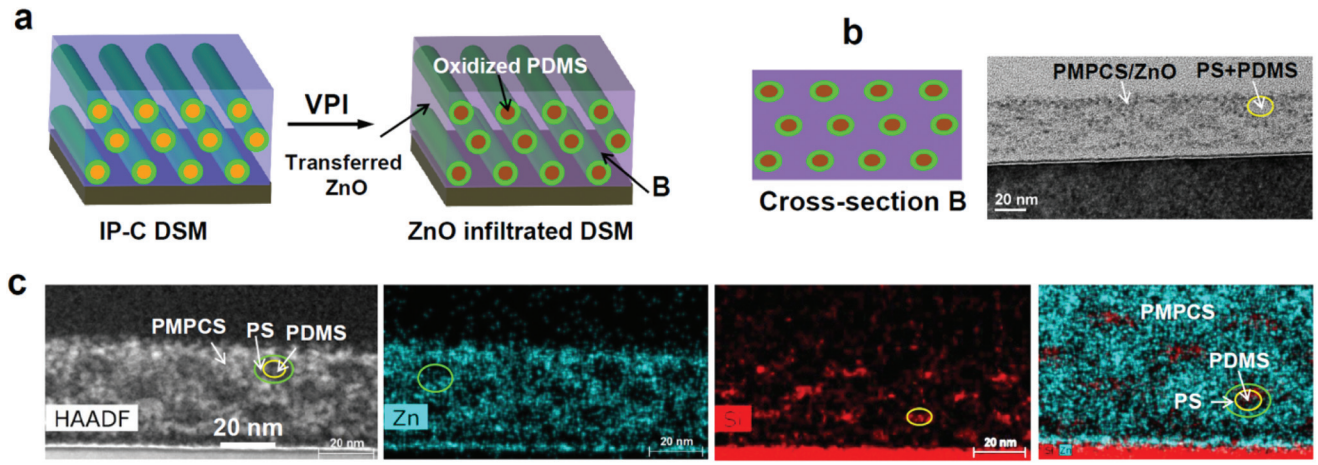

Fig. 3 (a) Schematic illustration of ZnO vapor-phase infiltration in the in-plane core–shell cylindrical morphology of DSM films, (b) structure in plane B and bright-field TEM image of the film after ZnO infiltration, and (c) HAADF STEM imaging and elemental mapping of the ZnO infiltrated films.

areas correspond to ZnO-infiltrated PMPCS and the bright oval regions correspond to the PS/PDMS cylinders. The cross-sectional HAADF STEM image and EDS mapping in Fig. 3c shows cross-sections of 3 layers of cylinders, and the spacing between the locations of the Zn and the Si indicates the shell of PS surrounding the PDMS cylinders. The oval shape of the cylinder cross-sections is a result of the deswelling which reduces the film thickness while preserving the in-plane cylinder spacing, and is consistent with the distortion factor of the HEX array. The cylinder-to-cylinder distance along the in-plane direction is 31 nm matching that observed in the top-view image.

As a comparison, the core–shell structure of the DSM triblock terpolymer was confirmed by TEM of a cross-section of a bulk sample without infiltration, Fig. S4.† The PDMS core appears dark due to its higher electron density. The PS shell (bright) and PMPCS matrix (grey) are clearly resolved after a short electron beam exposure, but increasing exposure time rapidly degrades the sample and blurs the contrast.

We also infiltrated ZnO into DSM films with hexagonally coordinated perforated lamella morphology. Although the etched films only present perforated lamellar oxidized-PDMS patterns (Fig. 1e), the HPL morphology is expected to consist of core–shell perforated lamellae (Fig. 4a). The cross-sectional bright-field TEM image of the ZnO infiltrated films show dark layers with perpendicular features representing the PMPCS/ZnO, consistent with the morphology of the cross-section along plane C of the HPL structure in Fig. 4a and b. Terracing of the films is

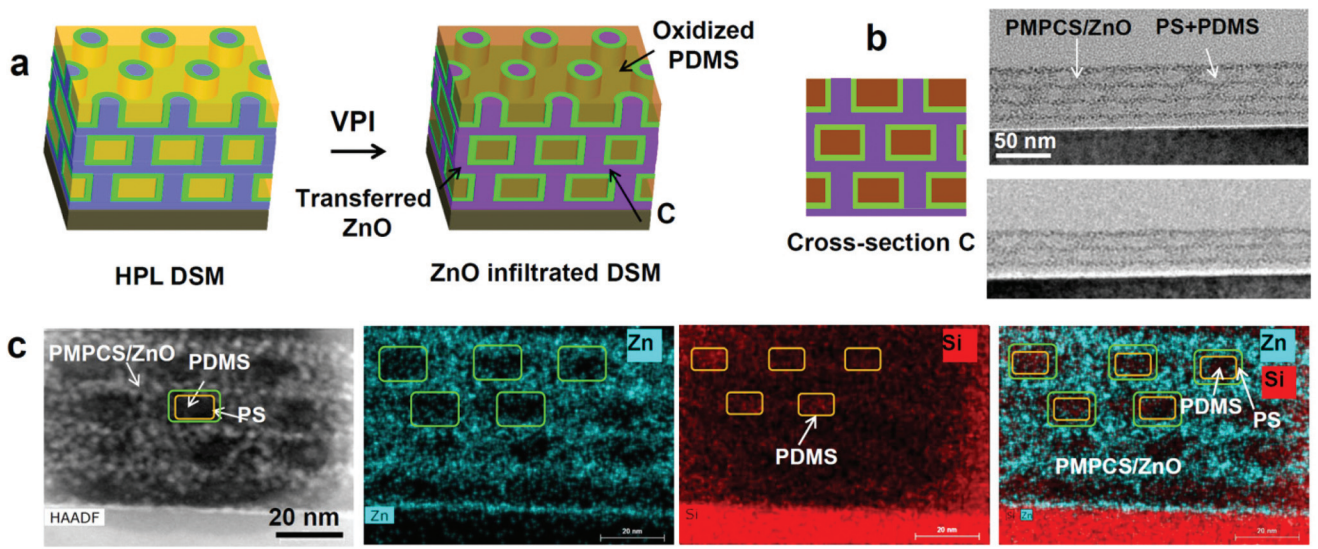

Fig. 4 (a) Schematic illustration of ZnO infiltration in the core–shell perforated lamellar structure of DSM films, (b) the cross-section plane C and cross-sectional bright-field TEM images of the films and (c) HAADF TEM image and elemental mapping.

also observed, Fig. S5b.† 4 layers and 3 layers of HPL morphology were observed in thicker and thinner regions of the film, Fig. 4b. Unlike the DSM IP-C, the HAADF STEM clearly shows ZnO infiltration in the PMPCS with the dark rectangular areas corresponding to the PS/PDMS microdomains, Fig. 4c. The EDS mapping shows Zn elements in the PMPCS domain, and the Si concentrated near the centers of the rectangular features. The spacing between Zn and Si indicates the PS shell (Fig. 4c). The perpendicular cylinder-cylinder distance is 37 nm, and the PMPCS/ZnO interlayer spacing is 16 nm. The ZnO infiltration therefore delineates the liquid crystal blocks with high selectivity and enables resolution of the core–shell structure.

The infiltration process is not limited to ZnO; other materials may be deposited within the PMPCS such as alumina using the TMA precursor. Liquid-phase processes may also be used to introduce inorganic species such as transition metals as has been demonstrated for poly(2vinylpyridine)- or poly(4vinylpyridine)-containing block copolymers.[8–10] However, an attempt to introduce Cu into the DSM triblock terpolymer from aqueous $CuCl_2$ was unsuccessful (Fig. S6†).

Conclusions

We demonstrate the domain-selective incorporation of ZnO within the PMPCS liquid crystalline microdomains of the DM diblock copolymer and DSM triblock terpolymer by using an SIS process. The ZnO is selectively and uniformly distributed in the PMPCS, and TEM confirms the core–shell morphology and 'three color' structures of the DSM. The improved infiltration selectivity and fidelity compared with our previous study highlights the benefits of placing appropriate reactive moieties into Si-containing BCP systems to obtain spatially resolved nanocomposite structures. The etch resistance of the PDMS block and the ZnO-infused PMPCS enable the fabrication of ZnO/SiO_x binary nanocomposites replicating the BCP ordered structures. DM and DSM liquid crystalline BCPs combine the advantages of silicon-containing BCPs and high infiltration selectivity with a wide range of available morphologies, and provide a route to fabrication of 3D hybrid nanomaterials by application of infiltration synthesis and etching.

Conflicts of interest

There are no conflicts to declare.

Acknowledgements

Financial support from NSF DMR-1606911 and the Applied Basic Research Program of Science and Technology Commission Foundation of Sichuan Province (Grants 2021YJ0559) are gratefully acknowledged. Shared experimental facilities of CMSE, an NSF MRSEC under award DMR-1419807, and the MIT NanoStructures Laboratory were used. This research was carried out in part at the Center for Functional Nanomaterials, which is a U.S. DOE Office of Science Facility, at Brookhaven National Laboratory under Contract No. DE-SC0012704. CAR and SL acknowledge support from the Semiconductor Research Corporation.

References

1 H. Ahn, S. Park, S.-W. Kim, P. J. Yoo, D. Y. Ryu and T. P. Russell, *ACS Nano*, 2014, **8**, 11745.
2 C. Cummins, T. Ghoshal, J. D. Holmes and M. A. Morris, *Adv. Mater.*, 2016, **28**, 5586.
3 F. S. Bates and G. H. Fredrickson, *Phys. Today*, 1999, **52**, 32.
4 C. Sinturel, F. S. Bates and M. A. Hillmyer, *ACS Macro Lett.*, 2015, **4**, 1044.
5 A. Tavakkoli K. G., K. W. Gotrik, A. F. Hannon, A. Alexander-Katz, C. A. Ross and K. K. Berggren, *Science*, 2012, **336**, 1294.
6 S. B. Darling, *Prog. Polym. Sci.*, 2007, **32**, 1152.
7 K. Nickmans and A. P. H. J. Schenning, *Adv. Mater.*, 2018, **30**, 1703713.
8 M. Aizawa and J. M. Buriak, *Chem. Mater.*, 2007, **19**, 5090.
9 J. Chai, D. Wang, X. N. Fan and J. M. Buriak, *Nat. Nanotechnol.*, 2007, **2**, 500.
10 S. K. Cha, J. H. Mun, T. Chang, S. Y. Kim, J. Y. Kim, H. M. Jin, J. Y. Lee, J. Shin, K. H. Kim and S. O. Kim, *ACS Nano*, 2015, **9**, 5536.
11 Q. Peng, Y. C. Tseng, S. B. Darling and J. W. Elam, *Adv. Mater.*, 2010, **22**, 5129.
12 A. Subramanian, N. Tiwale, G. Doerk, K. Kisslinger and C. Y. Nam, *ACS Appl. Mater. Interfaces*, 2020, **12**, 1444.
13 A. Subramanian, N. Tiwale and C.-Y. Nam, *JOM*, 2019, **71**, 185.
14 Q. Peng, Y. C. Tseng, S. B. Darling and J. W. Elam, *ACS Nano*, 2011, **5**, 4600.
15 A. J. M. Mackus, A. A. Bol and W. M. M. Kessels, *Nanoscale*, 2014, **6**, 10941.
16 J. Kamcev, D. S. Germack, D. Nykypanchuk, R. B. Grubbs, C.-Y. Nam and C. T. Black, *ACS Nano*, 2013, **7**, 339.
17 A. Rahman, P. W. Majewski, G. Doerk, C. T. Black and K. G. Yager, *Nat. Commun.*, 2016, **7**, 13988.
18 S. K. Cha, G. Y. Lee, J. H. Mun, H. M. Jin, C. Y. Moon, J. S. Kim, K. H. Kim, S.-J. Jeong and S. O. Kim, *ACS Appl. Mater. Interfaces*, 2017, **9**, 15727.
19 M. Ramanathan, Y. C. Tseng, K. Ariga and S. B. Darling, *J. Mater. Chem. C*, 2013, **1**, 2080.
20 J. Y. Kim, J. Lim, H. M. Jin, B. H. Kim, S.-J. Jeong, D. S. Choi, D. J. Li and S. O. Kim, *Adv. Mater.*, 2016, **28**, 1591.
21 G. G. Yang, J. Choi, S. K. Cha, G. Y. Lee, H. M. Jin, H. S. Hwang, T. Yun, J. Kang, K. H. Han, J. H. Kim, H. J. Choi, S. G. Im and S. O. Kim, *ACS Nano*, 2019, **13**, 13092.
22 M. Moshonov and G. L. Frey, *Langmuir*, 2015, **31**, 12762.
23 R. P. Padbury and J. S. Jur, *Langmuir*, 2014, **30**, 9228.

24 J. Yin, Q. Xu, Z. G. Wang, X. P. Yao and Y. Wang, *J. Mater. Chem. C*, 2013, **1**, 1029.
25 K. Aissou, M. Mumtaz, G. Fleury, G. Portale, C. Navarro, E. Cloutet, C. Brochon, C. A. Ross and G. Hadziioannou, *Adv. Mater.*, 2015, **27**, 261.
26 Y. Rho, K. Aissou, M. Mumtaz, W. Kwon, G. Pécastaings, C. Mocuta, S. Stanecu, E. Cloutet, C. Brochon, G. Fleury and G. Hadziioannou, *Small*, 2015, **11**, 6377.
27 T.-Y. Lo, M. R. Krishnan, K.-Y. Lu and R.-M. Ho, *Prog. Polym. Sci.*, 2018, **77**, 19.
28 K. Aissou, M. Mumtaz, P. Marcasuzaa, C. Brochon, E. Cloutet, G. Fleury and G. Hadziioannou, *Small*, 2017, **13**, 1603184.
29 J. W. Jeong, W. I. Park, M.-J. Kim, C. A. Ross and Y. S. Jung, *Nano Lett.*, 2011, **11**, 4095.
30 S. Lee, A. Subramanian, N. Tiwale, K. Kisslinger, M. Mumtaz, L.-Y. Shi, K. Aissou, C.-Y. Nam and C. A. Ross, *Chem. Mater.*, 2020, **32**, 5309.
31 L.-Y. Shi, Y. Zhou, X.-H. Fan and Z. Shen, *Macromolecules*, 2013, **46**, 5308.
32 L.-Y. Shi, C. Yin, B. Zhou, W. Xia, L. Weng and C. A. Ross, *Macromolecules*, 2021, **54**, 1657.
33 L.-Y. Shi, F. Liao, L.-C. Cheng, S. Lee, R. Ran, Z. Shen and C. A. Ross, *ACS Macro Lett.*, 2019, **8**, 852.
34 X.-F. Chen, Z. Shen, X.-H. Wan, X.-H. Fan, E.-Q. Chen, Y. Ma and Q.-F. Zhou, *Chem. Soc. Rev.*, 2010, **39**, 3072.
35 X. Lyu, A. Xiao, W. Zhang, P. Hou, K. Gu, Z. Tang, H. Pan, F. Wu, Z. Shen and X.-H. Fan, *Angew. Chem., Int. Ed.*, 2018, **57**, 10132.
36 L.-Y. Shi, J. Lan, S. Lee, L.-C. Cheng, K. G. Yager and C. A. Ross, *ACS Nano*, 2020, **14**, 4289.
37 L.-Y. Shi, Y. Pan, Q.-K. Zhang, Y. Zhou, X.-H. Fan and Z.-H. Shen, *Chin. J. Polym. Sci.*, 2014, **32**, 1524.
38 A. Subramanian, G. Doerk, K. Kisslinger, D. H. Yi, R. B. Grubbs and C. Y. Nam, *Nanoscale*, 2019, **11**, 9533.
39 L.-C. Cheng, K. R. Gadelrab, K. Kawamoto, K. G. Yager, J. A. Johnson, A. Alexander-Katz and C. A. Ross, *Nano Lett.*, 2018, **18**, 4360.
40 W. Bai, K. G. Yager and C. A. Ross, *Macromolecules*, 2015, **48**, 8574.